



Cite this: *Nanoscale*, 2019, **11**, 11660

Tunable photoluminescence and an enhanced photoelectric response of Mn^{2+} -doped $CsPbCl_3$ perovskite nanocrystals via pressure-induced structure evolution†

Junkai Zhang, ^a Sihang Ji, ^b Yanzhang Ma, ^c Renquan Guan, ^a Xiaoxin Wu, ^a Xin Qu, ^a Bingmin Yan, ^{*d} Dongzhou Zhang, ^e Jialong Zhao, ^{*a} and Jinghai Yang ^{*a}

Mn^{2+} : $CsPbCl_3$ nanocrystals (NCs) were synthesized using a modified one-pot injection method, which exhibits significantly improved thermal stability. For the first time, the pressure-treated optical and structural properties of synthetic Mn^{2+} : $CsPbCl_3$ NCs were further investigated, and their associated intriguing electrical and photoelectric properties were revealed from impedance spectra and photocurrent measurements under compression. The pressure-dependent photoluminescence experienced an initial redshift before 1.7 GPa followed by a continuous blueshift, as evidenced by the bandgap shifts. High-pressure XRD spectra uncovered a cubic-to-orthorhombic structural transition at about 1.1 GPa and subsequent amorphization upon further compression, which was fully reversible. Furthermore, the sample annealing from 340 K drove grain growth and decreased grain boundary resistance at ambient pressure. The compression further decreased the grain boundary barrier and improved the electrical conductivity (up to $\sim 10^{-2} \Omega^{-1} \text{ cm}^{-1}$) of the thermally annealed Mn^{2+} : $CsPbCl_3$ NC surface. Simultaneous photocurrent enhancement of thermally annealed NCs was also achieved as expected, and reached optimal performance at 0.7 GPa. Strikingly, after the pressure cycling (loading–releasing), the results show that thermally annealed Mn^{2+} : $CsPbCl_3$ NCs gained preservable higher electrical conductivity (~ 10 times increase) and an improved photoelectric response compared to the ambient state before compression. This work proves that high pressure is useful for opening the versatility in the structure and properties of metal–halide perovskite nanocrystals leading to a promising way for superior optoelectronic materials-by-design.

Received 9th April 2019,
Accepted 18th May 2019

DOI: 10.1039/c9nr03045j
rsc.li/nanoscale

^aKey Laboratory of Functional Materials Physics and Chemistry of the Ministry of Education, Jilin Normal University, Siping 136000, P. R. China.

E-mail: zhaqjl@ciomp.ac.cn, jhyang1@jlnu.edu.cn

^bDepartment of Physics, Jilin University, Changchun 130023, P. R. China

^cDepartment of Mechanical Engineering, Texas Tech University, Lubbock, TX 79409, USA

^dCenter for High Pressure Science and Technology Advanced Research, Beijing 100094, P. R. China. E-mail: bingmin.yan@hpstar.ac.cn

^eHawai'i Institute of Geophysics and Planetology, School of Ocean and Earth Science and Technology, University of Hawai'i at Manoa, Honolulu, Hawaii 96822, USA

†Electronic supplementary information (ESI) available: Sample assembly drawing; comparison of Van der Pauw model and the parallel-plate capacitor electrodes; indexed XRD pattern of as-synthesized Mn^{2+} : $CsPbCl_3$ NCs; Raman spectra at different pressures; time-dependent photocurrent of thermally annealed Mn^{2+} : $CsPbCl_3$ NCs; TEM and high-resolution TEM images of Mn^{2+} : $CsPbCl_3$ NCs (with/without thermal treatment) quenched from selected pressures in different high-pressure measurements. See DOI: [10.1039/c9nr03045j](https://doi.org/10.1039/c9nr03045j)

Introduction

$CsPbX_3$ ($X = Cl, Br, \text{ or } I$) metal–halide perovskite nanocrystals (NCs) have attracted significant attention in the fields of light emitting diodes (LEDs), lasers, photodetectors, solar cells and so forth. This is because of their superior optoelectric properties including narrow emission line widths, high photoluminescence quantum yield, broad spectral range covering visible luminescence, excellent and stable photosensitivity, and tunable electroluminescence.^{1–10} Impurity doping has been comprehensively explored to stabilize crystalline phases and tune the optoelectronic performance of different $CsPbX_3$ nanocrystals by virtue of optimum occupation of appropriately different elements in host lattices.^{3–5,11} Furthermore, it is often necessary to use nontoxic or less toxic elements, instead of Pb, for the purpose of practical applications of Pb-based nanocrystals.^{12,13}

Recently, highly luminescent manganese ion (Mn^{2+}) doping has been explored as a useful approach to monitor spectro-

scopic properties and structural stabilities of CsPbX_3 NCs.^{14–16} By varying the positions and concentrations of replaced dopants and the structures and sizes of the NCs,^{17–21} Mn^{2+} -doped NCs usually exhibit orange or red PL emission (derived from the $\text{Mn}^{2+} \text{ } ^4\text{T}_1 \rightarrow {}^6\text{A}_1$ transition) with high PL QYs (>50%) and large bandwidths (256–410 meV). Moreover, Mn^{2+} -doped NCs often possess longer excited-state lifetimes and better photochemical stabilities than their undoped counterparts.^{22–24} Meanwhile, the effect of temperature on Mn^{2+} -doped NC emission and a detailed understanding of the thermal degradation mechanism have also been well documented.^{15,23–25}

High pressure is an environmentally friendly, innovative approach that can radically tune the interatomic distance and electronic configuration, and the crystallographic and microstructural properties (like the crystal structure, micro-morphology, grain or grain boundary, and defects) of materials, facilitating the exploration of a variety of new physical and chemical characteristics.^{26–30} Therefore, the combination of high pressure and impurity doped NCs is expected to set off a brand-new route to modulate the structure and properties of CsPbX_3 -based materials.

Very recently, high-pressure research studies on pure CsPbX_3 materials have seen a new upsurge in interest.^{31–39} Zhang *et al.* consistently observed an orthogonal-to-orthogonal isostructural transition at moderate pressures (between 1.2 and 2.1 GPa), and subsequent amorphization of bulk CsPbBr_3 and bulk CsPbCl_3 upon compression, respectively.^{32,38} These results were ascribed to the bond-length decrease and the inorganic framework distortion due to the application of pressure. Meanwhile, the band-gap engineering under compression was found to rationalize the pressure-treated optical evolution of two samples. Furthermore, Xiao *et al.* carried out the pressure-induced carrier-lifetime prolongation of CsPbBr_3 NCs accompanied by band-gap narrowing during the isostructural phase transition in the ambient-pressure orthogonal phase.³⁵ Meanwhile, the effect of geometrical morphologies on the pressure interval of phase transitions and the band-gap changes was investigated under compressed CsPbBr_3 NCs, nanowires, nanocubes and their corresponding bulk counterparts.³⁵ In addition, the phase stabilities and the correlation between the optical properties and structural evolution of CsPbI_3 NCs and bulk samples have been reported successively.^{34,37,39}

Though great efforts have been put in studying crystallographic and electronic structures, and optical properties of CsPbX_3 samples under high pressure, there are still no reported results on the compressed properties of CsPbCl_3 NCs as well as impurity doped NCs. More importantly, to date, we inadequately understand how compression tunes the photoelectric response, for instance, the photocurrent, of CsPbX_3 NCs. CsPbX_3 materials have potential value in applications in photoelectricity. The insulating layer is formed by surface organic-ligands (such as OAm and OA) of CsPbX_3 NCs so that electron transport is prevented in the electrochemistry process.⁴⁰ The main problem is excessive surface ligands blocking probing for CsPbX_3 NCs' electrical conductivity. At present, high-pressure photoelectric studies are focused on

organometallic halide perovskites. The application of pressure has been proved to enhance the visible light response of MASnI_3 , MAPbI_3 , and MAPbBr_3 .^{41–44} However, the chemical instability and sensitivity to oxygen/water of organometallic halide perovskites limit actual photoelectric applications.^{45,46} Therefore, whether or not the photoelectric response of all-inorganic CsPbX_3 NCs can be enhanced by pressure, like the universal law for organometallic halide perovskites under compression, is highly expected to be revealed. Also, much work is needed to establish the structure–property relationship of CsPbX_3 NCs under compression. These aforementioned issues motivated us to conduct further high-pressure studies.

In this study, we applied pressure on $\text{Mn}^{2+}:\text{CsPbCl}_3$ NCs, one of the members of all-inorganic metal–halide perovskite nanosystems, exhibiting better thermodynamic stability. Firstly, absorption and PL spectroscopy studies were carried out to characterize the pressure-treated optical properties. Secondly, synchrotron radiation XRD spectra were collected to monitor the structural evolution under compression, which has still not been well-defined, and will, therefore, provide the basis for understanding the changes in pressure-tuned properties. Last but not least, photocurrent measurements were performed to study the pressure effect on the visible light response of $\text{Mn}^{2+}:\text{CsPbCl}_3$ NCs. Impedance spectra measurements were used to study electrical transport properties and grain boundary effects of the NCs under compression. The results not only clearly illustrate the modification mechanism of optical properties but also open up a promising strategy for the photoelectric improvement in all-inorganic CsPbX_3 -based applications.

Experimental section

$\text{Mn}^{2+}:\text{CsPbCl}_3$ NCs with a typical Mn^{2+} -doping concentration of 2.4% (relative to Pb^{2+}) were synthesized using an improved one-pot injection method, which was reported in our previous study.²³ The detailed descriptions of sample preparation, characterization and first-principles calculations⁴⁷ are seen in the ESI.† A symmetrical diamond anvil cell (DAC) with coupled diamond anvils with 400 μm culets was employed to generate high pressure. The schematic drawing of sample assembly, and parallel-plate and Van der Pauw electrodes^{48,49} is shown in Fig. S1 and S2, respectively, in the ESI.† The ruby fluorescence method was used as pressure calibration for all high-pressure experiments. Silicon oil was used as the pressure-transmitting medium for *in situ* high-pressure PL, absorption and XRD measurements. However, no pressure-transmitting medium was loaded into the sample chamber of electrical measurements to maintain the good contact interface between the sample and the probing electrodes.

In situ high-pressure PL spectra were collected with a Renishaw InVia spectrometer using a 325 nm continuous wave laser with an output power of 10 mW and a 50× Leica optical microscope. Absorption spectra were collected using an Ocean Optics QE65000 scientific-grade UV-vis spectrophotometer.

Synchrotron radiation XRD experiments were conducted at the 13-BM-C station of the Advanced Photon Source (APS), Argonne National Laboratory (ANL) ($\lambda = 0.406750 \text{ \AA}$). High-pressure impedance spectra were obtained using an impedance analyzer (Solartron 1260) in parallel with a dielectric interface (Solartron 1296). Photocurrent was recorded by using a CHI-760E electrochemical workstation. More details can be found in the ESI.[†]

Results and discussion

Fig. 1 shows the optical characteristics, crystal structure, and morphologies of $\text{Mn}^{2+}:\text{CsPbCl}_3$ NCs with 2.4% doping concentration under ambient conditions. The PL spectrum of Mn^{2+} :

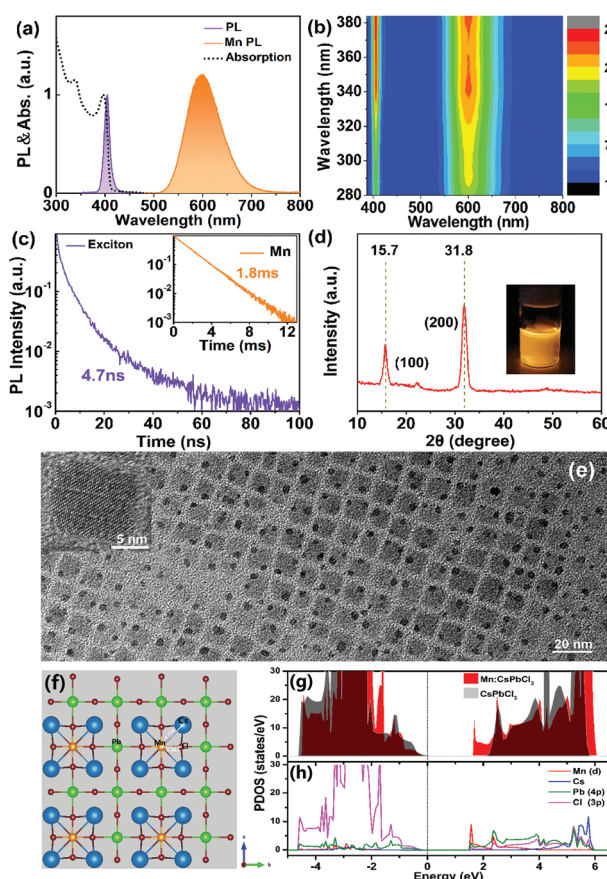


Fig. 1 (a) Absorption, PL, and (b) 2D PL excitation spectra of synthesized $\text{Mn}^{2+}:\text{CsPbCl}_3$ NCs with a typical Mn^{2+} -doping concentration of 2.4% (relative to Pb^{2+}). (c) Decay curve of the exciton emission. The inset of (c) is the decay curve of the Mn^{2+} emission. (d) XRD pattern of $\text{Mn}^{2+}:\text{CsPbCl}_3$ NCs. The inset of (d) is an image of the solution under the excitation of 365 nm wavelength, highlighting the prevailing orange color due to the Mn^{2+} ion emission. (e) The TEM image and the corresponding high-resolution TEM image. (f) Calculated 3D/three dimensional stacking diagram of $\text{Mn}^{2+}:\text{CsPbCl}_3$ by using the first-principles calculations. (g) Calculated total density of state (DOS) of pure CsPbCl_3 and $\text{Mn}^{2+}:\text{CsPbCl}_3$, respectively, in the framework of density functional theory (DFT) using the Vienna *ab initio* simulation package (VASP). (h) PDOS of $\text{Mn}^{2+}:\text{CsPbCl}_3$.

CsPbCl_3 NCs shows two distinct peaks, located at $\sim 404 \text{ nm}$ (violet) and $\sim 598 \text{ nm}$ (orange), respectively (Fig. 1a). The PL peak at $\sim 404 \text{ nm}$ is well ascribed to the host emission of the NCs and the one at $\sim 598 \text{ nm}$ is attributed to the $\text{Mn}^{2+} \text{ }^4\text{T}_1 \rightarrow {}^6\text{A}_1$ transition. Correspondingly, $\text{Mn}^{2+}:\text{CsPbCl}_3$ NCs show an obvious absorption edge at $\sim 396 \text{ nm}$, which corresponds to the exciton emission. The heterogeneity of the NCs was also examined. The energies of PL peaks remained nearly invariable as the excitation shifted from 300 to 385 nm gradually, indicating the negligible heterogeneity (Fig. 1b). Furthermore, the fluorescence lifetimes of the exciton and the Mn^{2+} dopant were monitored, respectively (Fig. 1c). The band-edge luminescence shows a short PL lifetime of 4.7 ns, which is in sharp contrast to the Mn^{2+} PL lifetime of 1.8 ms. The long PL lifetime of the Mn^{2+} ions originates from the parity-forbidden spin orbital ${}^4\text{T}_{1g} \rightarrow {}^6\text{A}_{1g}$ excitation of the Mn^{2+} dopant. Fig. 1d shows the XRD pattern of $\text{Mn}^{2+}:\text{CsPbCl}_3$ NCs, which crystallize in a cubic structure (#75-0411). Fig. 1e demonstrates the morphology of $\text{Mn}^{2+}:\text{CsPbCl}_3$ NCs and reveals their uniform size distribution (good dispersibility) and high crystallinity (clear lattice fringes). The average grain size of nanocrystals is $\sim 8.7 \text{ nm}$. Fig. 1f displays that smaller Mn^{2+} dopants instead of Pb^{2+} induce the non-hydrostatic lattice contraction of coordinate octahedra in the cubic phase of CsPbCl_3 . Such contractions may fundamentally stabilize $\text{Mn}^{2+}:\text{CsPbCl}_3$ NCs and bring in better thermal stability of high-quality Mn^{2+} -doped CsPbX_3 nanocrystals than their pure counterparts. The DOS reveals the form of an impurity band caused by Mn^{2+} dopants in CsPbCl_3 NCs. The conduction band bottom is obviously composed of the Pb (4p) and Cl (3p) hybridized orbits, and the Mn (d) isolated orbits. The results of calculation illustrate that the dual-color emission derives from the band-edge emission of host lattices in conjunction with the Mn^{2+} impurity excitation, as exemplified by Fig. 1g and h.

The pressure-tuned optical properties of synthesized $\text{Mn}^{2+}:\text{CsPbCl}_3$ NCs were monitored by means of *in situ* PL measurements. The representative steady-state PL spectra under compression are shown in Fig. 2a. The exciton and Mn^{2+} ion PL peaks both exhibit a visible redshift from the start of full pressurization to 1.7 GPa, followed by a continuous blueshift up to 4.5 GPa. The synchronized pressure changes of Mn^{2+} PL with one exciton are attributed to the crystal field transfer of energy levels because of the competitive efforts of host lattice shrinking and inorganic framework distortion under compression. The turning point ($\sim 1.7 \text{ GPa}$) of PL peak positions is likely to be related to an underlying pressure-induced structural phase transition of $\text{Mn}^{2+}:\text{CsPbCl}_3$ NCs. The initial PL intensities gradually weaken during compression and eventually disappear at approximately 4.5 GPa, coinciding with the occurrence of amorphous $\text{Mn}^{2+}:\text{CsPbCl}_3$ NCs, which can be well attributed to the enhanced recombination process in the amorphous phase. Upon full release of the pressure, the PL spectrum of $\text{Mn}^{2+}:\text{CsPbCl}_3$ NCs reappears, indicating that the sample transforms from amorphization to recrystallization under decompression. In comparison with the original state before compression, the exciton PL peak is relatively weakened and shifts

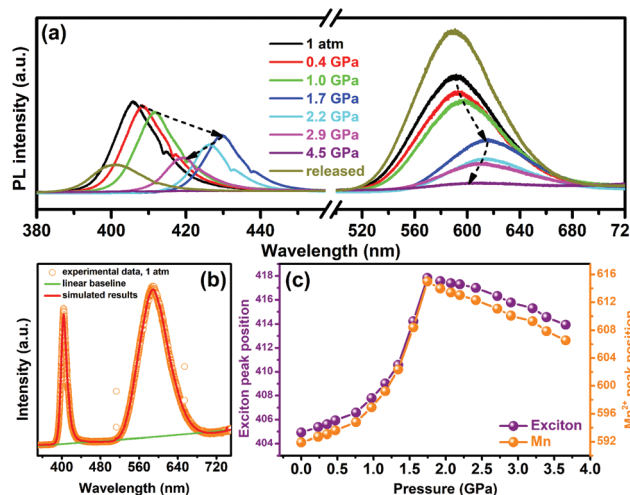


Fig. 2 (a) PL spectra versus pressure of the as-prepared $\text{Mn}^{2+}:\text{CsPbCl}_3$ NCs. The arrow symbols are guides for the eyes. (b) The representative PL spectrum at 1 atm with its corresponding profile fitting. (c) The pressure dependent PL peak positions of the exciton and Mn^{2+} ions, respectively.

into a lower wavelength of ~ 403 nm. Meanwhile, the Mn^{2+} PL peak is slightly enhanced after the pressure annealing (loading-releasing), which is mainly attributed to the pressure-induced self-defect increase and the grain size reduction. Moreover, the multi-peak Gaussian fitting (a case study of the PL spectrum at 1 atm) shows the $\text{Mn}^{2+}:\text{CsPbCl}_3$ NC PL peak wavelength *versus* pressure in Fig. 2c. It is evident that the discontinuities in the PL spectra shift occur at ~ 1.7 GPa.

Band gap evolution can adequately monitor unusual changes of optical and photoelectric properties under compression. Fig. 3a displays the band gaps of $\text{Mn}^{2+}:\text{CsPbCl}_3$ NCs at representative pressures, including 1 atm, 0.5 GPa, 1.4 GPa, and 2.2 GPa, as calculated *via* the extrapolation of the linear dynamics to the energy axis intercept by Tauc plots.⁵⁰ We surveyed the band gap (E_g) of the NCs regarding the Kubelka-Munk representation:

$$(\alpha h\nu)^2 = C(h\nu - E_g) \quad (1)$$

where α is the absorption coefficient and C is the edge width parameter. The plot of the pressure-dependent E_g is clearly shown in Fig. 3b. When the pressure is increased up to 1.1 GPa, E_g first experiences a narrowing by approximately 0.02 eV. With further increasing pressure, E_g decreases obviously from 2.82 eV to 2.70 eV. According to previously reported literature studies^{35,38,39} and our results, the redshift of the band gap is mainly attributed to the increased overlap of Pb–Cl electron clouds due to the Pb–Cl bond shrinkage, which compensates for the effect induced by the octahedral tilting and twisting in this pressure regime. When subjected to a pressure of ~ 1.8 GPa, E_g abruptly increases with pressure, which originates from the structure transformation and is attributed to the decreased coupling between Cl 3p and Pb 6s orbitals by the $[\text{PbCl}_6]^{4-}$ octahedral distortion. Besides, E_g shows a temporary

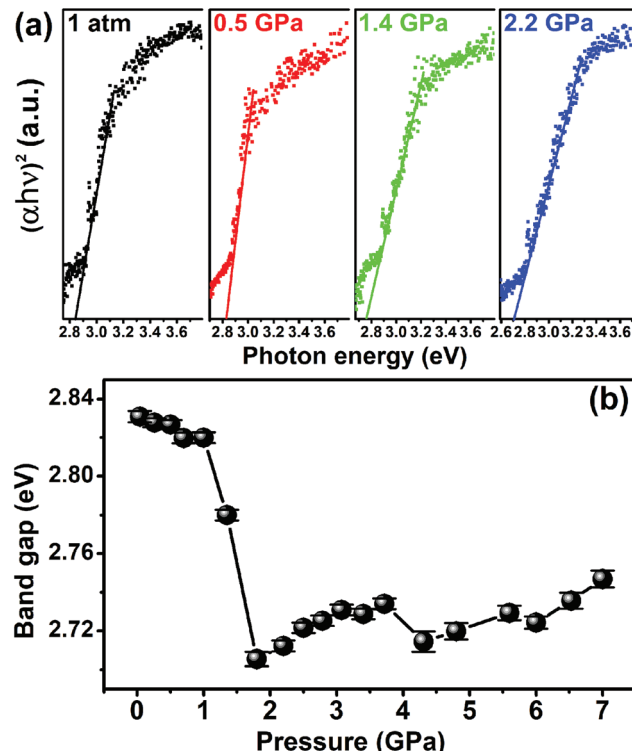


Fig. 3 (a) Band gaps of $\text{Mn}^{2+}:\text{CsPbCl}_3$ NCs at representative pressures estimated by Tauc plots, respectively. (b) The variation of band gap with pressure.

dip between 3.7 GPa and 4.3 GPa, which is likely caused by the appearance of amorphization in the sample.

Pressure can effectively manipulate the characteristics of nanocrystals *via* modifying the crystal structures of NCs (*i.e.*, different polymorphs) and their packing efficiencies and patterns.^{33,51–55} In this work, the hard NC core ($\text{Mn}^{2+}:\text{CsPbCl}_3$) is covered by a soft organic-ligand shell (OAm and OA). The structural modification of $\text{Mn}^{2+}:\text{CsPbCl}_3$ NCs under compression was monitored by using *in situ* synchrotron radiation XRD measurements (Fig. 4). Based on the collected XRD data at 1 atm, the indexed results clearly show an ambient-pressure cubic phase in $\text{Mn}^{2+}:\text{CsPbCl}_3$ NCs, which was identified with previously reported results (more details in ESI Fig. S3†). As the pressure gradually increases, no considerable changes occur in the diffraction peaks below 1.1 GPa, except that the peaks gradually shift towards high-angles, indicative of a pressure-induced uniform shrinkage of NCs and surface ligands. $[\text{PbCl}_6]^{4-}$ includes regular octahedral networks for cubic $\text{Mn}^{2+}:\text{CsPbCl}_3$, exhibiting a contraction with the increase in pressure. However, four new diffraction peaks at $\sim 4.6^\circ$, $\sim 8.9^\circ$, $\sim 9.4^\circ$, and $\sim 9.7^\circ$ suddenly emerge at pressures between 1.1 GPa and 1.3 GPa, which signifies the beginning of a structural phase transition. This is mainly attributed to the fact that a small magnitude of deviatoric stress is produced above critical pressure, which is able to deform the NCs into a distorted, non-cubic structure (*e.g.* orthorhombic). The $[\text{PbCl}_6]^{4-}$ octahedra undergo a stark distortion to accommodate the Jahn-

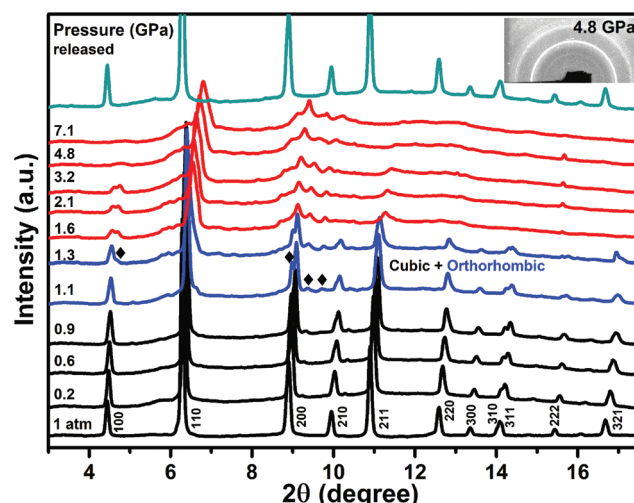


Fig. 4 Representative XRD patterns of $\text{Mn}^{2+}:\text{CsPbCl}_3$ NCs at different pressures. The \blacklozenge symbols present the newly emerged peaks of the high-pressure orthorhombic phase. The XRD pattern at 1 atm is well indexed into the cubic structure (space group: $Pm\bar{3}m$).

Teller effect upon further compression. Above 1.6 GPa, the phase transition is complete, and no further transformation is observed up to 7.1 GPa, the highest pressure covered by our experiments. Our observations are different from the previously reported reference,³⁸ which indicate that ambient-phase CsPbCl_3 (indexed to an orthorhombic structure) underwent an isostructural phase transition when the pressure reached 2.1 GPa. Besides, the diffraction peaks of the $\text{Mn}^{2+}:\text{CsPbCl}_3$ sample broaden obviously with further compression exceeding 4.8 GPa, which illustrates that the crystallinity of the NCs deteriorates and the sample tends to be amorphous with further increasing pressures. When the pressure is fully released, the crystal structure of the NCs recovers to the original cubic phase. The phase transition is fully reversible. In contrast to before compression, the morphology and crystallinity of the NCs do not exhibit a great change after the full release of pressure, except for the anisotropically oriented assignment of NCs and the obvious decrease of the inter-NC distance. These can be readily deduced from the TEM image (ESI Fig. S4†). Furthermore, the cycling process (crystallization–amorphization–recrystallization) is confirmed by the use of *in situ* Raman spectra measurements on $\text{Mn}^{2+}:\text{CsPbCl}_3$ NCs (ESI Fig. S5†).

The Rietveld profile fitting for the diffraction peak at 1 atm shows a good fit between the observed and calculated results using the cubic $Pm\bar{3}m$ space group, as evidenced by the tiny discrepancy factors ($R_p = 2.3\%$, $R_{wp} = 3.6\%$, see Fig. 5a). Lattice parameters are resolved to be $a = 5.595 (3)$ Å. In Fig. 5b, the Rietveld refinement at 1.6 GPa shows evidence that the best agreement between the observed and calculated results is achieved by considering that the new high-pressure phase is an orthorhombic phase ($R_p = 2.1\%$, $R_{wp} = 3.4\%$). The pressure dependent volume and lattice parameters are further determined by XRD refinements and geometry optimization,

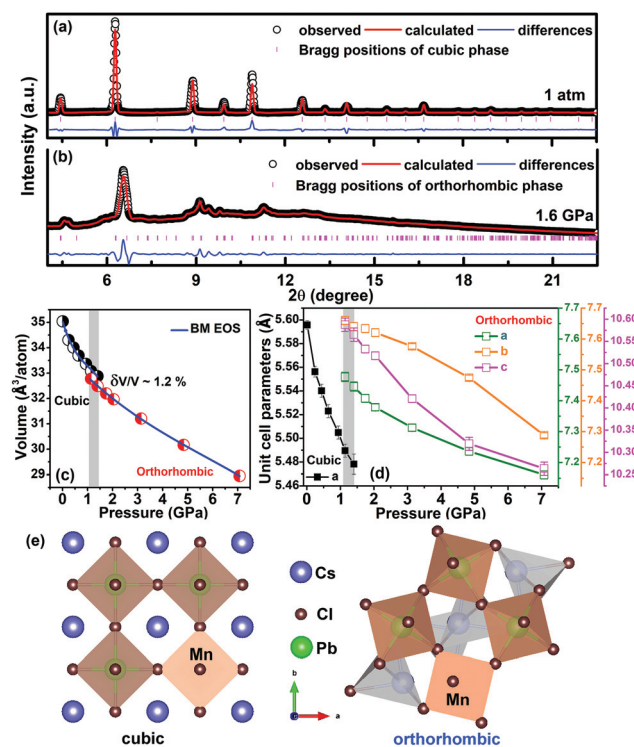


Fig. 5 Rietveld refinements of the ambient-pressure cubic phase at 1 atm (a) and the high-pressure orthorhombic phase at 1.6 GPa (b), respectively. Volume (c) and lattice parameters (d) against pressures in the cubic and orthorhombic phases, respectively. (e) Structural schematic diagrams of $\text{Mn}^{2+}:\text{CsPbCl}_3$ NCs.

respectively (Fig. 5c and d). It is found that the pressure-induced phase transition causes a slight increase of density by approximately 1.2% in $\text{Mn}^{2+}:\text{CsPbCl}_3$ NCs, as a consequence of the volume collapse. With B'_0 fixed at 4, B_0 in the orthorhombic phase is estimated to be 38.8 (6) GPa, which is much larger than the one in the cubic phase (15.2 (3) GPa). This indicates the high difficulty of compressibility towards the high-pressure phase. Besides, the compressibility is found to be obviously anisotropic in the orthorhombic phase. The b -axis is the most compressible. The phase transition involves the rearrangement of atoms and molecules in the structure cell. The ligand of the cations consequently changes from uniform octahedral to coexistent octahedral and dodecahedral in the high-pressure orthorhombic phase, see Fig. 5e.

Previous studies demonstrate that the heating-enabled electrical conductivity of the Pt_3Co nanocube was accomplished because of the formation of an NC-interconnected architecture at high temperature.⁵⁶ In this work, temperature treatment acts as a driving force that develops the size growth of $\text{Mn}^{2+}:\text{CsPbCl}_3$ NCs and the removal of more surface ligands from the NCs. As shown in Fig. 6a, firstly, both the host and the Mn^{2+} PL emissions of $\text{Mn}^{2+}:\text{CsPbCl}_3$ NCs shift to a longer wavelength with thermal treatment at 340 K compared to those of the original NCs, implying the obvious growth of thermally annealed nanocrystals. Secondly, the PL intensities of

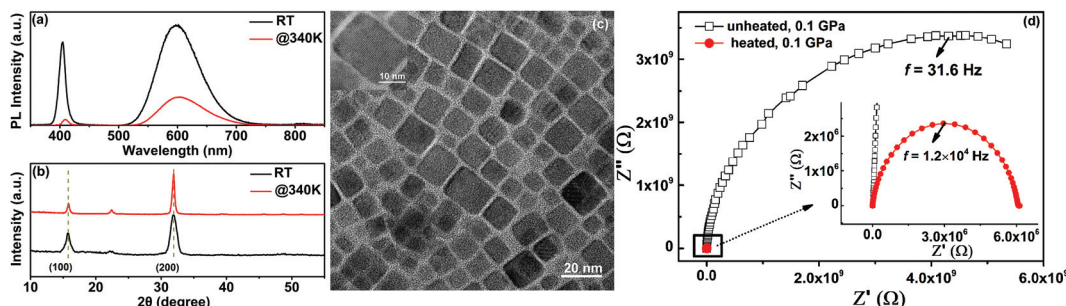


Fig. 6 (a) PL and (b) XRD spectra of Mn^{2+} : $CsPbCl_3$ NCs without/with thermal treatment at 340 K for 20 min in argon. The PL and XRD data of the samples were collected when they were cooled to room temperature. (c) The TEM image of thermally annealed Mn^{2+} : $CsPbCl_3$ NCs annealed from 340 K. (d) Nyquist plots of the impedance spectra of Mn^{2+} : $CsPbCl_3$ NCs (open black squares) and thermally annealed Mn^{2+} : $CsPbCl_3$ NCs (solid red balls) at 0.1 GPa.

thermally annealed Mn^{2+} : $CsPbCl_3$ NCs are significantly reduced, which originates from the formation of nonradiative recombination defects on the NC surface on account of the considerable growth of the NCs at 340 K.^{23,25} In Fig. 6b, XRD patterns indicate that thermally annealed Mn^{2+} : $CsPbCl_3$ NCs have a cubic structure with good crystallinity. Moreover, the diffraction peaks show remarkable narrowing because of the increase in the NC size. Consistently, the growth of the NC size is clearly monitored in the TEM image for a random selection of the NCs (Fig. 6c). Besides, after temperature treatment, due to the Ostwald ripening effect, the small Pb° seeds that remain decorating the regrowing crystals gradually fuse on the surface of Mn^{2+} : $CsPbCl$ NCs and do not leave observable enrichments (seem like black dots in the TEM image) within the oriented attached perovskite particles. On the other hand, thermal treatment is intended to optimize ligand density at the surface of the NCs due to the grain-size changes. We performed impedance spectra measurements to reveal the effects of the thermal annealing process on the electrical transport properties of powdered Mn^{2+} : $CsPbCl_3$ NCs. The semicircle diameter in impedance spectra estimates the value of electron-transfer resistance. Without annealing, excessive surface ligands result in assembled nanocrystals with bad carrier injection and electric transportation, as shown in Fig. 6c. By contrast, thermally annealed NCs have proper electrical conductivity without destroying ink stability, because of the apparent decrease in ligands induced by the temperature effect (shown in the inset of Fig. 6c).

Pressure can effectively improve the electrical conductivity (*i.e.*, increase carrier concentration or mobility) of nanomaterials by modulating their grain interior and the grain boundary barrier. Fig. 7a and b show the Nyquist plots of impedance spectra of compressed Mn^{2+} : $CsPbCl_3$ NCs and thermally annealed NCs, respectively, which reveal only one complete semicircle at selected pressures. In our previous coverage on bulk materials (such as NaN_3 ⁵⁷ and $BaTeO_3$ ⁵⁸), two independent semicircles can be distinguished in the Z'' & Z' planes, describing the grain (bulk) and grain boundary (surface) effect on transport of charge carriers, respectively. We believe that in this case, compared to their corresponding bulk

counterparts, nanomaterials have specific properties such as the small size effect, confinement effect and grain boundary effect. The semicircles in the impedance spectra of Mn^{2+} : $CsPbCl_3$ nanocrystals represent the dominant contribution of their grain boundaries on the total electrical transportation, referring to boundary sliding and dislocation, and reconstruction on the NC surface.

The model of the equivalent circuit generally reliably demonstrates the interface dynamic behaviors of powder samples. The parallel capacitance (CPE) and resistance (R_{gb}) exist in the equivalent circuit of the impedance, which are useful analogues to evaluate the grain boundary relaxation. In Fig. 7c, the agreement of the simulated spectra with the experimental data further indicates the validity of considering the RC conduction in thermally annealed Mn^{2+} : $CsPbCl_3$ NCs. Meanwhile, both electrical conductivities (σ_{gb} and σ_{un}) of thermally annealed Mn^{2+} : $CsPbCl_3$ NCs and original NCs, respectively, are deduced from impedance spectra results (Fig. 7d) by using the equation of $\sigma = L/RS$ where L is the Mo electrode distance; R is the sample resistance; S is the detecting window area. As shown in Fig. 7d, σ_{gb} is $\sim 5 \times 10^{-4} \Omega^{-1} \text{ cm}^{-1}$ at the beginning of compression (~ 0.1 GPa). Subsequently, σ_{gb} increases quickly by about one order of magnitude when the pressure is increased up to 1.2 GPa, followed by a smooth increase up to $9.8 \times 10^{-3} \Omega^{-1} \text{ cm}^{-1}$ between 1.2 GPa and 3.7 GPa. The apparent discontinuity in electrical properties of thermally annealed Mn^{2+} : $CsPbCl_3$ NCs correlates with the structural phase transition between 1.1 GPa and 1.6 GPa. Upon decompression, σ_{gb} gradually decreases with releasing pressure but persists in the value of $\sim 5 \times 10^{-3} \Omega^{-1} \text{ cm}^{-1}$ at 0.2 GPa. The results show that thermally annealed NCs gain preservable higher conductive characteristics after the pressure cycling (loading–releasing). On the other hand, the values of σ_{un} always remain within $3.4 \times 10^{-7} \Omega^{-1} \text{ cm}^{-1}$ and $5.3 \times 10^{-7} \Omega^{-1} \text{ cm}^{-1}$ with the increase of pressure up to 7.0 GPa. Without annealing, the electrical conductivity of original NCs is almost pressure-independent because of the poor conductivity of the surface ligands (OAm and OA). Excessive ligands form an insulating layer and prevent the transportation of electrons among the grains.

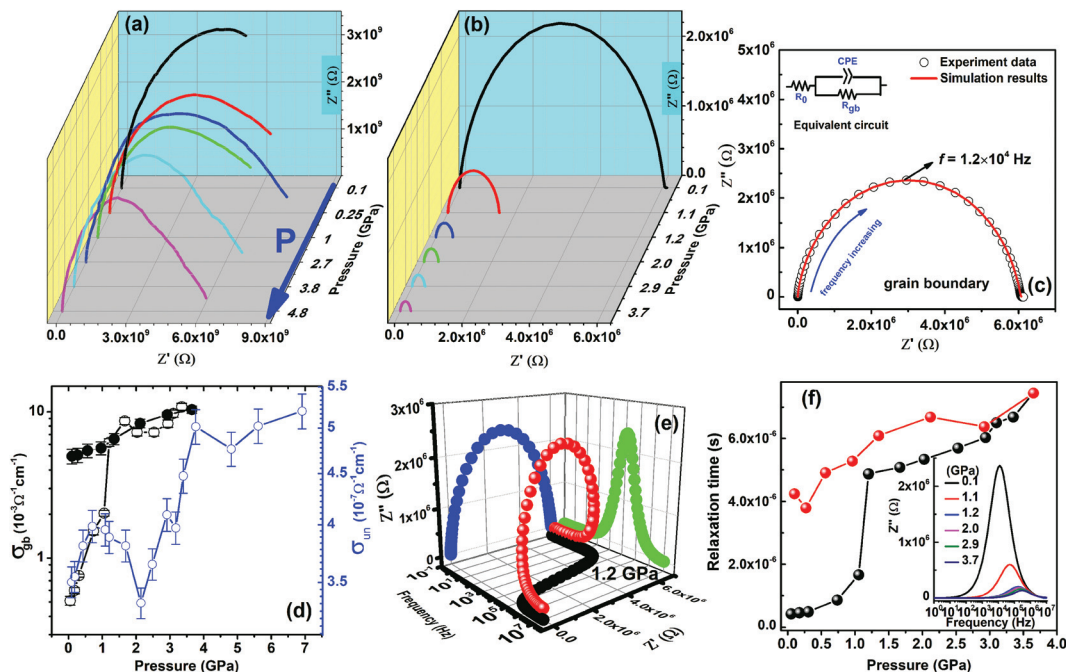


Fig. 7 Nyquist plots of impedance spectra of $\text{Mn}^{2+}:\text{CsPbCl}_3$ NCs (a) and thermally annealed NCs (b) at selected pressures. (c) The impedance spectrum of thermally annealed $\text{Mn}^{2+}:\text{CsPbCl}_3$ NCs at 0.1 GPa with simulation to a commonly RC equivalent circuit (in inset, R_0 , contact resistance, R_{gb} , grain boundary resistance, CPE, double-layer capacitance). (d) Pressure-dependent R_{gb} (open black balls) of thermally annealed $\text{Mn}^{2+}:\text{CsPbCl}_3$ NCs and R_{un} (open blue balls) of the original sample, respectively. (e) 3D impedance spectrum (Z' , Z'' and frequency) of thermally annealed $\text{Mn}^{2+}:\text{CsPbCl}_3$ NCs at 1.2 GPa. (f) Pressure-dependent relaxation time (τ). The inset of (f) is the impedance imaginary against frequency at representative pressures.

The electrical conductivity of nanomaterials is generally associated with the length of the carriers' relaxation time (τ) in the transportation at the grain boundaries. As an example, the 3D-perspective plots of impedance spectra of thermally annealed $\text{Mn}^{2+}:\text{CsPbCl}_3$ NCs at 1.2 GPa are illustrated in Fig. 7e. By the observation of the projection to the Z'' & frequency plane, the relaxation peak (f_{\max}) of the grain boundary is clearly observed at a certain pressure. Thus, the value of τ should be deduced ($\tau = 1/f_{\max}$), and correspondingly, its pressure dependence is shown in Fig. 7f. The compression effectively reduces the carriers' relaxation time to half compared to before the phase transition (the blueshift of f_{\max} towards the higher-frequencies is found with increasing pressure, as shown in the inset of Fig. 7f). The carrier transport and conductivity mechanism in the grain boundary is as follows: because of the random packing of NC surface defects, the unsaturated coordinated atoms are inhomogeneous at the grain boundaries and the barrier height is very high. Upon compression, the effective grain boundary area of space-charge distribution is increased because the contact between the grains has improved considerably, and thus, the energy barrier formed in carrier transportation is reduced. Meanwhile, no pressure-transmitting medium is loaded into the sample chamber of electrical measurements for maintaining the good contact interface between the sample and the probing electrodes. This sample loading approach enables a rapid generation of pressure gradient and more deviatoric stress *via* deforming the gasket sample chamber.⁵¹ Under higher deviatoric stress

resulting from the increased pressure, the chemical bonding between ligands and NCs may be gradually broken. New types of organic/inorganic interfaces (*i.e.*, grain boundaries) are generated in designer solids and drive the active surface atoms to move around, eliminating defects and tacking faults, and filling voids. The capacity of charge bounding is reduced, and the scattering for carriers is weakened, concerning the dangling bonds with pressure. To sum up, the compression produces an expected increase of σ_{gb} , accompanying the step decrease in τ . Upon the full release of pressure, the $\text{Mn}^{2+}:\text{CsPbCl}_3$ NCs become sintered into a mesoscale ceramic form, which rationalizes the preservable electrical properties quenched from the compression into ambient conditions (ESI Fig. S6†). The electrical conductivity of thermally annealed $\text{Mn}^{2+}:\text{CsPbCl}_3$ NCs is effectively enhanced, as expected, by using several combined means of pressure-modulated crystallographic and electronic structures.

Due to the existence of the long-chain organic surface ligands (*i.e.*, OA and OAm), the highly insulating properties of powdered $\text{Mn}^{2+}:\text{CsPbCl}_3$ NCs occur in the dark or under visible light (shown in Fig. 8a). After annealing in argon at 340 K, the electrical conductivity of thermally annealed $\text{Mn}^{2+}:\text{CsPbCl}_3$ NCs is proven to increase considerably. Correspondingly, thermally annealed NCs show better photoelectric characteristics, as expected, when the photocurrent increases sharply as the light is turned on and then drops rapidly to the original value as the light is turned off (Fig. 8a). To further explore the potential application of CsPbX_3 (X = Cl,

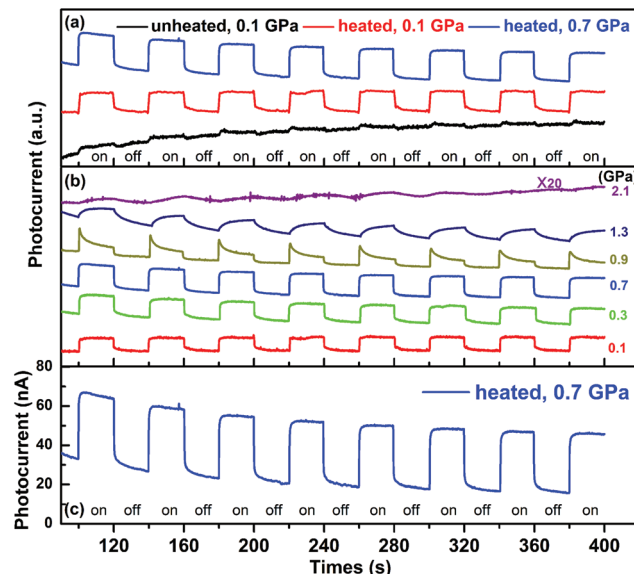


Fig. 8 (a) Time-dependent photocurrent of Mn^{2+} : CsPbCl_3 NCs without thermal treatment at 0.1 GPa (black line) and thermally annealed Mn^{2+} : CsPbCl_3 NCs at 0.1 GPa (red line) and 0.7 GPa (blue line) measured in the dark and under visible light, respectively. (b) The photocurrent of thermally annealed Mn^{2+} : CsPbCl_3 NCs at selected pressures. (c) The detailed photocurrent-time response of thermally annealed NCs at 0.7 GPa. In addition, (a–c) show the dynamic photoresponse behavior over multiple cycles of white light radiation (3 W cm^{-2}).

Br, or I) NCs in optoelectronic devices, we conducted *in situ* photocurrent measurements on thermally annealed Mn^{2+} : CsPbCl_3 NCs under compression (Fig. 8b). The sample exhibits an apparent response to the white light between 0.1 and 1.2 GPa as the switch turns on and off, repeatedly. In particular, the ratio of the photocurrent to dark current shows a near doubling due to the application of external pressure, 0.7 GPa, which is comparable to the photonic responsiveness at 0.1 GPa. A positive pressure effect on the photoelectric properties is observed. When the pressure exceeds the critical value of 2.1 GPa, the photocurrent can hardly be detected. This is attributed to the partial amorphization of the nano-grains induced by too much pressure. Fig. 8c shows the details of the best photoelectric properties of thermally annealed NCs at 0.7 GPa. The reproducible and prompt photocurrent response to the multiple on/off cycles indicates the excellent optical switching and stability of thermally annealed Mn^{2+} : CsPbCl_3 NCs for potential application in photodetectors.

Furthermore, it is essential whether or not the photocurrent enhancement of thermally annealed Mn^{2+} : CsPbCl_3 NCs generated by compression can be preserved when the pressure quenches under ambient conditions. The photocurrent of the sample quenched from 0.7 GPa is found to be still slightly increased in comparison with the state at the beginning of compression (ESI Fig. S7†). In comparison, the photocurrent quenched from 2.1 GPa becomes very weak and lacks stability and a reproducible photoresponse to the multiple on/off cycles. The cubic-to-orthorhombic phase transition of Mn^{2+} :

CsPbCl_3 NCs is fully reversible after pressure cycling. Thus, the structural evolution during compression/decompression should not be the key to addressing this difference. The difference is likely attributed to the amorphization of local grains in the quenched sample from relatively high pressures (*i.e.*, 2.1 GPa), which can be readily deduced from the high-resolution TEM images (ESI Fig. S8†). The amorphization from higher pressure generates more defects, which accelerates the recombination of the electron and the hole, and decreases the concentration of charge carriers in the electrical transport process. Therefore, the photocurrent is hardly detected in the samples quenched from high pressure exceeding 2.1 GPa. Based on the above high-pressure studies, it can be expected that the photoelectric conversion performance of all inorganic CsPbX_3 ($X = \text{Cl}, \text{Br}, \text{or I}$) perovskite nanocrystal-based devices could be further improved *via* artificial stress treatment, such as chemical doping, lattice-mismatched fabricating, and high-temperature and high-pressure synthesis.

Conclusion

This work demonstrates that the optical properties and structural evolution of Mn^{2+} : CsPbCl_3 perovskite nanocrystals can be expertly tuned by using compression as a clean physical tool, and reveals the fundamental understanding of the structure–property relationship under high-pressure. More strikingly, the higher charge transport abilities and enhanced photoelectric response are generated by quenching from mild pressure to ambient conditions. Our results reveal the high potential of pressure-treated all-inorganic CsPbX_3 ($X = \text{Cl}, \text{Br}, \text{or I}$) metal-halide perovskite materials for a broad range of applications.

Conflicts of interest

There are no conflicts to declare.

Acknowledgements

This work was supported by the National Natural Science Foundation of China (Grant No. 51608226, 11847126, 21801092, 21878119, 21776110, and 61775081) and the Thirteenth Five-Year Program for Science and Technology of Education Department of Jilin Province (Item No. JJKH20191004KJ and JJKH20180769KJ).

References

- Q. A. Akkerman, G. Rainó, M. V. Kovalenko and L. Manna, Challenges and Opportunities for Colloidal Lead Halide Perovskite Nanocrystals, *Nat. Mater.*, 2018, **17**, 394–405.
- C. Jia, H. Li, L. F. Tan, X. W. Meng, J. B. Gao and H. B. Li, Observation and Implication of Halide Exchange beyond

- CsPbX₃ Perovskite Nanocrystals, *Nanoscale*, 2019, **11**, 3123–3128.
- 3 M. V. Kovalenko, L. Protesescu and M. I. Bodnarchuk, Properties and Potential Optoelectronic Applications of Lead Halide Perovskite Nanocrystals, *Science*, 2017, **358**, 745–750.
- 4 L. L. Fei, X. Yuan, J. Hua, M. Ikezawa, R. S. Zeng, H. B. Li, Y. Masumoto and J. L. Zhao, Enhanced Luminescence and Energy Transfer in Mn²⁺ doped CsPbCl_{3-x}Br_x Perovskite Nanocrystals, *Nanoscale*, 2018, **10**, 19435–19442.
- 5 H. Shao, X. Bai, H. N. Cui, G. C. Pan, P. T. Jing, S. N. Qu, J. Y. Zhu, Y. Zhai, B. Dong and H. W. Song, White Light Emission in Bi³⁺/Mn²⁺ Ion Co-Doped CsPbCl₃ Perovskite Nanocrystals, *Nanoscale*, 2018, **10**, 1023–1029.
- 6 N. J. Keun, C. D. Hyung, R. R. J. Kyu, L. J. Hwan and P. J. Hyeok, Methodologies toward Efficient and Stable Cesium Lead Halide Perovskite-Based Solar Cells, *Adv. Sci.*, 2018, **5**, 1800509.
- 7 W. Zhai, J. Lin, C. Li, S. M. Hu, Y. Huang, C. Yu, Z. K. Wen, Z. Y. Liu, Y. Fang and C. C. Tang, Solvothermal Synthesis of Cesium Lead Halide Perovskite Nanowires with Ultra-High Aspect Ratios for High-Performance Photodetectors, *Nanoscale*, 2018, **10**, 21451–21458.
- 8 Z. Long, H. Ren, J. H. Sun, J. Ouyang and N. Na, High-Throughput and Tunable Synthesis of Colloidal CsPbX₃ Perovskite Nanocrystals in a Heterogeneous System by Microwave Irradiation, *Chem. Commun.*, 2017, **53**, 9914–9917.
- 9 d. Yang, M. H. Cao, Q. X. Zhong, P. L. Li, X. H. Zhang and Q. Zhang, All-Inorganic Cesium Lead Halide Perovskite Nanocrystals: Synthesis, Surface Engineering and Applications, *J. Mater. Chem. C*, 2019, **7**, 757–789.
- 10 K. Park, J. W. Lee, J. D. Kim, N. S. Han, D. M. Jang, S. Jeong, J. Park and J. K. Song, Light-Matter Interactions in Cesium Lead Halide Perovskite Nanowire Lasers, *J. Phys. Chem. Lett.*, 2016, **7**, 3703–3710.
- 11 D. Q. Chen and X. Chen, Luminescent Perovskite Quantum Dots: Synthesis, Microstructures, Optical Properties and Applications, *J. Mater. Chem. C*, 2019, **7**, 1413–1446.
- 12 Y. Zhai, X. Bai, G. C. Pan, J. Y. Zhu, H. Shao, B. Dong, L. Xu and H. W. Song, Effective Blue-Violet Photoluminescence through Lanthanum and Fluorine Ions Co-Doping for CsPbCl₃ Perovskite Quantum Dots, *Nanoscale*, 2019, **11**, 2484–2491.
- 13 T. Cai, H. J. Yang, K. Hills-Kimball, J. P. Song, H. Zhu, E. Hofman, W. W. Zheng, B. M. Rubenstein and O. Chen, Synthesis of All-Inorganic Cd-Doped CsPbCl₃ Perovskite Nanocrystals with Dual-Wavelength Emission, *J. Phys. Chem. Lett.*, 2018, **9**, 7079–7084.
- 14 T. Qiao, D. Parobek, Y. T. Dong, E. Ha and D. H. Son, Photoinduced Mn Doping in Cesium Lead Halide Perovskite Nanocrystals, *Nanoscale*, 2019, **11**, 5247–5253.
- 15 S. Zou, Y. Liu, J. Li, C. Liu, R. Feng, F. Jiang, Y. Li, J. Song, H. Zeng, M. Hong and X. Chen, Stabilizing Cesium Lead Halide Perovskite Lattice through Mn(II) Substitution for Air-Stable Light-Emitting Diodes, *J. Am. Chem. Soc.*, 2017, **139**, 11443–11450.
- 16 W. Stam, J. J. Geuchies, T. Altantzis, K. H. W. Bos, J. D. Meeldijk, S. V. Aert, S. Bals, D. Vanmaelbergh and C. M. Donega, Highly Emissive Divalent-Lon-Doped Colloidal CsPb_{1-x}M_xBr₃ Perovskite Nanocrystals through Cation Exchange, *J. Am. Chem. Soc.*, 2017, **139**, 4087–4097.
- 17 H. Liu, Z. Wu, J. Shao, D. Yao, H. Gao, Y. Liu, W. Yu, H. Zhang and B. Yang, CsPb_xMn_{1-x}Cl₃ Perovskite Quantum Dots with High Mn Substitution Ratio, *ACS Nano*, 2017, **11**, 2239–2247.
- 18 W. Liu, Q. Lin, H. Li, K. Wu, I. Robel, J. M. Pietryga and V. I. Klimov, Mn²⁺-Doped Lead Halide Perovskite Nanocrystals with Dual-Color Emission Controlled by Halide Content, *J. Am. Chem. Soc.*, 2016, **138**, 14954–14961.
- 19 D. Parobek, B. J. Roman, Y. Dong, H. Jin, E. Lee, M. Sheldon and D. H. Son, Exciton-to-Dopant Energy Transfer in Mn-Doped Cesium Lead Halide Perovskite Nanocrystals, *Nano Lett.*, 2016, **16**, 7376–7380.
- 20 A. K. Guria, S. K. Dutta, S. D. Adhikari and N. Pradhan, Doping Mn²⁺ in Lead Halide Perovskite Nanocrystals: Successes and Challenges, *ACS Energy Lett.*, 2017, **2**, 1014–1021.
- 21 V. S. Chirvony, S. González-Carrero, I. Suárez, R. E. Galian, M. Sessolo, H. J. Bolink, J. P. Martínez-Pastor and J. Pérez-Prieto, Delayed Luminescence in Lead Halide Perovskite Nanocrystals, *J. Phys. Chem. C*, 2017, **121**, 13381–13390.
- 22 A. De, N. Mondal and A. Samanta, Luminescence Tuning and Exciton Dynamics of Mn-Doped CsPbCl₃ Nanocrystals, *Nanoscale*, 2017, **9**, 16722–16727.
- 23 X. Yuan, S. Ji, M. C. De Siena, L. Fei, Z. Zhao, Y. Wang, H. Li, J. Zhao and D. R. Gamelin, Photoluminescence Temperature Dependence, Dynamics, and Quantum Efficiencies in Mn²⁺-Doped CsPbCl₃ Perovskite Nanocrystals with Varied Dopant Concentration, *Chem. Mater.*, 2017, **29**, 8003–8011.
- 24 X. Yuan, J. Zheng, R. Zeng, P. Jing, W. Ji, J. Zhao, W. Yang and H. Li, Thermal Stability of Mn²⁺ Ion Luminescence in Mn-Doped Core-Shell Quantum Dots, *Nanoscale*, 2014, **6**, 300–307.
- 25 S. H. Ji, X. Yuan, J. Li, J. Hua, Y. J. Wang, R. S. Zeng, H. B. Li and J. L. Zhao, Photoluminescence Lifetimes and Thermal Degradation of Mn²⁺-Doped CsPbCl₃ Perovskite Nanocrystals, *J. Phys. Chem. C*, 2018, **122**, 23217–23223.
- 26 Z. W. Ma, Z. Liu, S. Y. Lu, L. R. Wang, X. L. Feng, D. W. Yang, K. Wang, G. J. Xiao, L. J. Zhang, S. A. T. Redfern and B. Zou, Pressure-Induced Emission of Cesium Lead Halide Perovskite Nanocrystals, *Nat. Commun.*, 2018, **9**, 4506.
- 27 J. K. Zhang, Y. L. Zhang, X. X. Wu, Y. Z. Ma, S. Y. Chien, R. Q. Guan, D. Z. Zhang, B. Yang, B. M. Yan and J. H. Yang, Correlation between Structural Changes and Electrical Transport Properties of Spinel ZnFe₂O₄ Nanoparticles under High Pressure, *ACS Appl. Mater. Interfaces*, 2018, **10**, 42856–42864.

- 28 Q. L. Wang, Y. Z. Ma, D. D. Sang, X. L. Wang, C. L. Liu, H. Q. Hu, W. J. Wang, B. Y. Zang, Q. L. Fan, Y. H. Han and C. X. Gao, Ionic Conduction in Sodium Azide under High Pressure: Experimental and Theoretical Approaches, *Appl. Phys. Lett.*, 2018, **112**, 173903.
- 29 S. Y. Lu, G. J. Xiao, L. Z. Sui, T. L. Feng, X. Yong, S. J. Zhu, B. J. Li, Z. Y. Liu, B. Zou, M. X. Jin, J. S. Tse, H. Yan and B. Yang, Piezochromic Carbon Dots with Two-photon Fluorescence, *Angew. Chem.*, 2017, **129**, 1–6.
- 30 L. Zhang, L. W. Wu, K. Wang and B. Zou, Pressure-Induced Broadband Emission of 2D Organic-Inorganic Hybrid Perovskite $(\text{C}_6\text{H}_5\text{C}_2\text{H}_4\text{NH}_3)_2\text{PbBr}_4$, *Adv. Sci.*, 2019, **6**, 1801628.
- 31 B. M. Ilyas and B. H. Elias, A Theoretical Study of Perovskite CsXCl_3 ($\text{X}=\text{Pb, Cd}$) within First Principles Calculations, *Phys. B*, 2017, **510**, 60–73.
- 32 L. Zhang, Q. X. Zeng and K. Wang, Pressure-Induced Structural and Optical Properties of Inorganic Halide Perovskite CsPbBr_3 , *J. Phys. Chem. Lett.*, 2017, **8**, 3752–3758.
- 33 Y. Nagaoka, K. Hills-Kimball, R. Tan, R. P. Li, Z. W. Wang and O. Chen, Nanocube Superlattices of Cesium Lead Bromide Perovskites and Pressure-Induced Phase Transformations at Atomic and Mesoscale Levels, *Adv. Mater.*, 2017, **29**, 1606666.
- 34 G. Yuan, S. Qin, X. Wu, H. R. Ding and A. H. Lu, Pressure-Induced Phase Transformation of CsPbI_3 by X-ray Diffraction and Raman Spectroscopy, *Phase Transitions*, 2018, **91**, 38–47.
- 35 G. J. Xiao, Y. Cao, G. Y. Qi, L. R. Wang, C. Liu, Z. W. Ma, X. Y. Yang, Y. M. Sui, W. T. Zheng and B. Zou, Pressure Effects on Structure and Optical Properties in Cesium Lead Bromide Perovskite Nanocrystals, *J. Am. Chem. Soc.*, 2017, **139**, 10087–10094.
- 36 Y. R. Ying, X. Luo and H. T. Huang, Pressure-Induced Topological Non-Trivial Phase and Tunable Optical Properties in All-Inorganic Halide Perovskites, *J. Phys. Chem. C*, 2018, **122**, 17718–17725.
- 37 J. C. Beimborn, L. M. G. Hall, P. Tongying, G. Dukovic and J. M. Weber, Pressure Response of Photoluminescence in Cesium Lead Iodide Perovskite Nanocrystals, *J. Phys. Chem. C*, 2018, **122**, 11024–11030.
- 38 L. Zhang, L. R. Wang, K. Wang and B. Zou, Pressure-Induced Structural Evolution and Optical Properties of Metal-Halide Perovskite CsPbCl_3 , *J. Phys. Chem. C*, 2018, **122**, 15220–15225.
- 39 Y. Cao, G. Y. Qi, C. Liu, L. R. Wang, Z. W. Ma, K. Wang, F. Du, G. J. Xiao and B. Zou, Pressure-Tailored Band Gap Engineering and Structure Evolution of Cubic Cesium Lead Iodide Perovskite Nanocrystals, *J. Phys. Chem. C*, 2018, **122**, 9332–9338.
- 40 Z. X. Cai, F. M. Li, W. Xu, S. J. Xia, J. B. Zeng, S. G. He and X. Chen, Colloidal CsPbBr_3 Perovskite Nanocrystal Films as Electrochemiluminescence Emitters in Aqueous Solutions, *Nano Res.*, 2018, **11**, 1447–1455.
- 41 T. Ou, J. Yan, C. Xiao, W. Shen, C. Liu, X. Liu, Y. Han, Y. Ma and C. Gao, Visible Light Response, Electrical Transport, and Amorphization in Compressed Organolead Iodine Perovskites, *Nanoscale*, 2016, **8**, 11426–11431.
- 42 X. Lü, Y. Wang, C. C. Stoumpos, Q. Hu, X. Guo, H. Chen, L. Yang, J. S. Smith, W. Yang, Y. Zhao, H. W. Xu, M. G. Kanatzidis and Q. X. Jia, Enhanced Structural Stability and Photo Responsiveness of $\text{CH}_3\text{NH}_3\text{SnI}_3$ Perovskite via Pressure-Induced Amorphization and Recrystallization, *Adv. Mater.*, 2016, **28**, 8663–8668.
- 43 M. Szafrański and A. Katrusiak, Mechanism of Pressure-Induced Phase Transitions, Amorphization, and Absorption-Edge Shift in Photovoltaic Methylammonium Lead Iodide, *J. Phys. Chem. Lett.*, 2016, **7**, 3458–3466.
- 44 H. C. Yan, T. J. Ou, H. Jiao, T. Y. Wang, Q. L. Wang, C. L. Liu, X. Z. Liu, Y. H. Han, Y. Z. Ma and C. X. Gao, Pressure Dependence of Mixed Conduction and Photo Responsiveness in Organolead Tribromide Perovskites, *J. Phys. Chem. Lett.*, 2017, **8**, 2944–2950.
- 45 J. Yang, B. D. Siempelkamp, D. Liu and T. L. Kelly, Investigation of $\text{CH}_3\text{NH}_3\text{PbI}_3$ Degradation Rates and Mechanisms in Controlled Humidity Environments using *in situ* Techniques, *ACS Nano*, 2015, **9**, 1955–1963.
- 46 N. Aristidou, C. Eames, I. Sanchez-Molina, X. N. Bu, J. Kosco, M. S. Islam and S. A. Haque, Fast Oxygen Diffusion and Iodide Defects Mediate Oxygen Induced Degradation of Perovskite Solar Cells, *Nat. Commun.*, 2017, **8**, 15218.
- 47 G. Kresse and J. Furthmüller, Efficient Iterative Schemes for ab Initio Total-Energy Calculations using a Plane-Wave Basis Set, *Phys. Rev. B: Condens. Matter Mater. Phys.*, 1996, **54**, 11169–11186.
- 48 C. Gao, Y. Han, Y. Ma, A. White, H. Liu, J. Luo, M. Li, C. He, A. Hao and X. Huang, Accurate Measurements of High Pressure Resistivity in a Diamond Anvil Cell, *Rev. Sci. Instrum.*, 2005, **76**, 083912.
- 49 Q. L. Wang, C. L. Liu, Y. H. Han, C. X. Gao and Y. Z. Ma, The Determination of Ionic Transport Properties at High Pressures in a Diamond Anvil Cell, *Rev. Sci. Instrum.*, 2016, **87**, 123904.
- 50 J. Tauc, R. Grigorovici and A. Vancu, Optical Properties and Electronic Structure of Amorphous Germanium, *Phys. Status Solidi B*, 1966, **15**, 627.
- 51 J. Zhu, Z. Quan, C. Wang, X. Wen, Y. Jiang, J. Fang, Z. Wang, Y. Zhao and H. Xu, Structural Evolution and Mechanical Behaviour of Pt Nanoparticle Superlattices at High Pressure, *Nanoscale*, 2016, **8**, 5214–5218.
- 52 H. Wu, F. Bai, Z. Sun, R. E. Haddad, D. M. Boye, Z. Wang, J. Y. Huang and H. Fan, Nanostructured Gold Architectures Formed through High Pressure-Driven Sintering of Spherical Nanoparticle Arrays, *J. Am. Chem. Soc.*, 2010, **132**, 12826–12828.
- 53 T. Wang, R. P. Li, Z. W. Quan, W. S. Loc, W. A. Bassett, H. W. Xu, Y. C. Cao, J. Y. Fang and Z. W. Wang, Pressure Processing of Nanocube Assemblies Toward Harvesting of a Metastable PbS Phase, *Adv. Mater.*, 2015, **27**, 4544–4549.
- 54 Z. W. Wang, C. Schliehe, T. Wang, Y. Nagaoka, Y. C. Cao, W. A. Bassett, H. M. Wu, H. Y. Fan and H. Weller,

- Deviatoric Stress Driven Formation of Large Single-Crystal PbS Nanosheet from Nanoparticles and in Situ Monitoring of Oriented Attachment, *J. Am. Chem. Soc.*, 2011, **133**, 14484–14487.
- 55 Y. C. Lin, W. C. Chou, A. S. Susha, S. V. Kershaw and A. L. Rogach, Photoluminescence and Time-Resolved Carrier Dynamics in Thiol-Capped CdTe Nanocrystals under High Pressure, *Nanoscale*, 2013, **5**, 3400–3405.
- 56 J. Zhang, J. L. Zhu, R. P. Li, J. Y. Fang and Z. W. Wang, Entropy-Driven Pt₃Co Nanocube Assembles and Thermally Mediated Electrical Conductivity with Anisotropic Variation of the Rhombohedral Superlattice, *Nano Lett.*, 2017, **17**, 362–367.
- 57 Q. L. Wang, Y. Z. Ma, D. D. Sang, X. L. Wang, C. L. Liu, H. Q. Hu, W. J. Wang, B. Y. Zhang, Q. L. Fan, Y. H. Han and C. X. Gao, Ionic Conduction in Sodium Azide under High Pressure: Experimental and Theoretical Approaches, *Appl. Phys. Lett.*, 2018, **112**, 173903.
- 58 D. D. Sang, Q. L. Wang, B. Y. Zhang, W. J. Wang and H. Q. Hu, Role of the Grain Boundaries on the Electrical Transport Behavior of Nanocrystalline BaTiO₃ under High Pressure, *Nat. Sci.*, 2018, **31**, 50–55.